MANUSCRIPT

Development of intensified flat-plate packed-bed solar reactors for heterogeneous photocatalysis

Bruno Ramos [a,b], João Gabriel M Carneiro [a], Leandro Issamu Nagamati [a], Antonio Carlos SC Teixeira [a]

[a] *Research Group in Advanced Oxidation Processes (AdOx), Dept. of Chemical Engineering, Polytechnic School, University of São Paulo, 05088000, São Paulo, Brazil*
[b] *Laboratory of Ceramics Processing, Department of Metallurgical and Materials Engineering, Polytechnic School, University of São Paulo, 05088000, São Paulo, Brazil*

Abstract. Solar-driven photocatalysis is a promising water-cleaning and energy-producing technology that addresses some of the most urgent engineering problems of the 21st century: universal access to potable water, use of renewable energy, and mitigation of CO_2 emissions. In this work, we aim at improving the efficiency of solar-driven photocatalysis by studying a novel reactor design based on microfluidic principles using 3D-printable geometries. The printed reactors had a dimensional accuracy of 97%, at a cost of less than \$1 per piece. They were packed with 1.0-mm glass and steel beads coated with ZnO synthesised by a sol-gel routine, resulting in a bed with 46.6% void fraction (reaction volume of ca. 840 µL and equivalent flow diameter of 580 µm) and a specific surface area of 3200 $m^2\ m^{-3}$. Photocatalytic experiments, under sunlight-level UV-A irradiation, showed that reactors packed with steel supports had apparent reaction rates ca. 75% higher than those packed with glass supports for the degradation of an aqueous solution of acetaminophen; however, they were strongly deactivated after the first use suggesting poor fixation. Glass supports showed no measurable deactivation after three consecutive uses. The apparent first-order reaction rates constants were between $1.9–9.5 \times 10^{-4}\ s^{-1}$, ca. ten times faster than observed for conventional slurry reactors. The mass transfer was shown to be efficient ($Sh > 7.7$) despite the catalyst being immobilised onto fixed substrates. Finally, the proposed reactor design has the merit of a straightforward scaling out by sizing the irradiation window according to design specifications, as exemplified in the paper.

Keywords: *photocatalysis; microfluidic reactors; 3D printing; packed bed reactor; fixed bed; process intensification; catalyst immobilization*

Corresponding author

Bruno Ramos (PhD)

bruno.ramos@usp.br

Tel: +55 11 3091 2262

1. INTRODUCTION

Photochemical reactors can be made in several configurations and shapes (Nguyen and Wu 2018). Among them, *plate reactors* – those in which the reaction medium flows between two parallel plates – are particularly suitable for harnessing solar energy, thanks to the combination of constant irradiated area and usually narrow optical pathways, leading to a consistent availability of photons throughout the reaction space. Along with the dimension of the interstitial space between the plates, their shapes will determine the fluid dynamics of the reactor; its mixing properties and residence time distributions. There are two main classes of fabrication processes that can be used to modify a plate structure at the micro-scale level: subtractive and additive processes (Ehrfeld et al. 2000). Examples of subtractive methods, based on the removal of material from the modified surface, include mechanical micromachining (Chen et al. 2019) and laser ablation (Lippert 2005; Beausoleil et al. 2020). Additive manufacture (AM) encompasses a group of technologies collectively known as *3D-printing* (Au et al. 2016), among which the fused filament fabrication (FFF) is the best known and the most widely used inside and outside scientific research (Sculpteo 2019). Unlike the subtractive techniques, AM modifies a surface by adding layers of materials with impressive dimensional control down to tenths of micrometres.

In addition to a carefully designed photoreactor, solar-based photochemical processes use additional species with improved energy-harnessing properties to use sunlight efficiently. These additives can be dispersed homogeneously in the reaction medium, such as the combined solar/Fenton processes (Nogueira et al. 2012; Khandarkhaeva et al. 2019); or can be supplied in a different phase, as is the case of solar/O_3 (Chávez et al. 2016) or the so-called heterogeneous photocatalysis.

Typical heterogeneous photocatalysts include metal oxide semiconductors, such as TiO_2, CdS or Fe_2O_3. The electronic band structure of these materials helps extend the photogenerated electron-hole pair lifetime by preventing instantaneous recombination, thereby allowing sufficient time for these reactive species to migrate towards the catalyst surface and promote redox reactions with adsorbed species (Kumar and Rao 2017).

A photocatalytic process necessarily involves the following steps: (i) reactant(s) adsorption onto the catalyst surface sites; (ii) photon absorption by the catalyst; (iii) electronic excitation and formation of electron-hole pairs; and (iv) electron transfer between the catalyst and the adsorbed species. Depending on the band energy correspondence between the catalyst and the adsorbed species, the latter might be reduced (an electron acceptor) or oxidised (an electron donor). This change in the electronic structure of activated species might trigger either a reaction with another species adsorbed in a neighbouring site on the catalyst surface; or a reaction with a species in the reaction media after desorption from the catalyst surface (Ohtani 2010). Whatever the role the activated species takes in the redox cycle promoted by the photogenerated electron-hole pairs, it is clear that the efficiency of the photocatalytic process is highly dependent upon mass transport conditions. Hence, a suitable reactor design becomes a major factor in the viability of these processes.

In this work, we present a rationale for the design of heterogeneous photoreactors, which is applied for the fabrication of a flat-plate packed-bed reactor. We do this by exploring (i) the configuration of the flow distributing region; and (ii) the technology used for prototyping the selected designs. Next, the reactors are evaluated for their performance regarding the photocatalytic removal of a model pharmaceutical pollutant (acetaminophen) in aqueous solution, under UV-A irradiation adjusted to match terrestrial sunlight levels. For this evaluation, two selected materials (glass and stainless steel) were used as supports for the photocatalyst (ZnO).

2. DESIGN RATIONALE

Considering the steps involved in heterogeneous photocatalysis, a suitable photocatalytic solar reactor design should mind the following guidelines:

A. Maximise the catalytic SSA (specific surface area);
B. Maximise the ISA (irradiated surface area);
C. Maximise photon absorption;
D. Minimise back-mixing;
E. Ensure a highly-controllable flow profile;
F. Ensure homogeneous catalyst distribution;
G. Minimise catalyst loss;
H. Minimise catalyst deactivation;
I. Minimise energy costs;
J. Minimise mass transport resistance;
K. Ensure ease of maintenance.

Following these guidelines requires collaborative work in different fields of engineering. The design of a heterogeneous catalytic reactor typically involves looking for a compromise between mass transport and economics. While some researches are devoted at optimising *slurry reactors*, i.e. reactors in which the photocatalyst is suspended in the reaction media, we have focused on *fixed-bed reactors*, where the catalyst is immobilised onto larger substrates that occupy fixed positions inside the reaction volume. **Table 1** summarises the well-known stronger and weaker points of both configurations (Van Gerven et al. 2007; Braham and Harris 2009; McCullagh et al. 2011).

Table 1.

Comparison between features of slurry and fixed-bed reactors for heterogeneous photocatalysis. Overall better (○), worse (×) or equivalent (△).

Guideline	Slurry	Fixed-bed

A	○	×
B	○	×
C	△	△
D	△	△
E	△	△
F	×	○
G	×	○
H	×	○
I	×	○
J	○	×
K	×	○

The weakest points of fixed-bed reactors lie in guidelines A, B and J. To overcome these limitations, we explored in this work two key properties from microfluidics (Kockmann 2008): (i) high surface-to-volume ratios; and (ii) short and precisely defined mass transfer lengths. By making use of these properties, it should be possible to minimise the natural impacts on SSA and mass transport brought about by shifting from slurry to fixed-bed operation (van Grieken et al. 2009). To achieve a microfluidic-like profile, we immobilise the photocatalyst onto 1.0-mm beads instead of the inner walls of the reactor. In this way, the beads provide obstacles to the flow, which should improve external mass transport by changing the flow velocity field (Tidona et al. 2012). The reactor design developed in this work focused on (i) the effect of the design of the inlet distribution channel; (ii) the impact of the fabrication technique; and (iii) the impact of the material of the supporting beads onto the reactor performance.

3. EXPERIMENTAL APPROACH

Reactor design optimisation. Selected reactor designs were drawn in 2D computer-aided design tools (AutoCAD 2019, Autodesk Inc.) and prototyped in PMMA by CO_2 laser ablation (Rujie, RJ-1060). Plates of 4.0-mm width were engraved at a constant speed of 70 mm s^{-1} and a maximum power of 40% (24 W), to provide a constant engraving depth of 2.0 mm throughout the marked design, such as shown in **Fig. 1**. After prototyping, the central rectangular space was brushed, polished with a silicon carbide polishing wheel (Dremel 4000, Robert Bosch GmbH), and sonicated for 1 h in distilled water to remove incrusted PMMA powder. As shown in **Fig. 1**, the diverse designs aimed at exploring different flow distribution geometries for constant channel widths (1.0 mm). The machined plates were enclosed by a clear top plate to allow for visual inspection of the flow by M3 bolts and nuts.

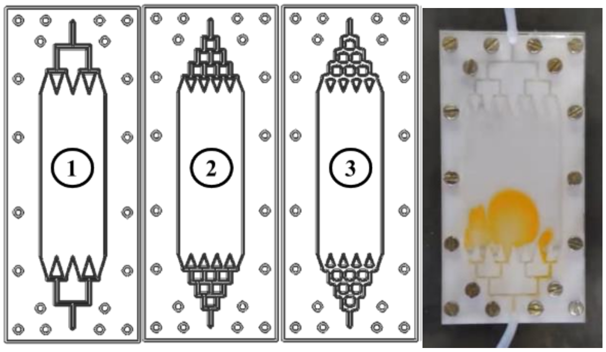

Fig. 1. Selected plate designs (1 to 3), and example of the assembled reactor with transparent covering and connections.

Final reactor prototype. A chosen reactor design, among the three shown in **Fig. 1**, was used as a base for a 3D-model prototyped in acrylonitrile butadiene styrene (ABS) by FFF in a desktop 3D printer (Creator Pro, Flashforge Co. Ltd.), using a proprietary slicing software (FlashPrint, Flashforge Co. Ltd.). Filament extrusion was carried out at 230 °C onto a heated bed (110 °C) at a speed of 60 mm s^{-1} in layers of 100 µm with a filling of 90%. An illumination window (76 × 26 × 1.2-mm soda-lime glass slide) was installed onto the ABS prototype and fixed with UV-resistant acetoxy silicone adhesive (Tekbond, Saint-Gobain S.A.).

Prototype quality and hydrodynamics. The quality of the machined plates was evaluated by confocal microscopy (DCM 3D, Leica Microsystems). Their dimensional accuracy and precision were evaluated by taking calibrated measurements of selected facets in an image analyser (Digimizer v.5.4.4, MedCalc Software Ltd.). The effect of the plate design on the flow pattern was evaluated in the empty reactors (i.e. without packing) by one-pulse residence time distribution (RTD) experiments using a saturated methyl orange aqueous solution as a tracer (Ramos et al. 2018). Tracer quantification was carried by UV-Vis spectroscopy (Cary 50, Varian Inc.) connected inline after the reactor outlet, with continuous sampling at 462 nm.

Catalyst immobilisation. Two support materials were chosen to make up the reactor bed: soda-lime glass (Sigma-Aldrich) and austenitic stainless steel (SUS) AISI 316 (Taian Xinxin Import & Export Co. Ltd.) spherical beads with 1.0-mm average diameter. The beads were washed thoroughly with distilled water and dried overnight in a laboratory oven (60 °C) before the catalyst immobilisation procedure. A sol-gel process was used to make the zinc oxide precursor suspension, following a common procedure reported in the literature (Aslan et al. 2004) with some modifications. 200 mg of zinc acetate dihydrate (P.A., Synth) was dissolved in 10 mL isopropyl alcohol (HPLC Standard, Merck) and 105 mg diethanolamine (P.A., Sigma-Aldrich) under continuous stirring at 50 °C. 1 mL of deionised water was then added dropwise to that solution, via a syringe pump (Elite 11, Harvard Apparatus), for 30 min. The solution turned cloudy white and viscous, after which the colloidal suspension was removed from heating. The beads (3 mL, tapped) were placed inside a spherical mesh, which was immersed in the precursor suspension where it remained under continuous magnetic stirring for 30 min. Next, the beads were taken out of the mesh and transferred to a crucible and into a furnace where they were fired for 3 h at 400 °C without gas purging. The immersion and calcination processes were repeated twice. At the end of the third and last calcination steps, the beads were washed thoroughly under running deionised water to remove excess ZnO powder, dried for 24 h at 60 °C, and stored in a hermetic recipient at room temperature.

Catalyst characterisation. The beads and the deposited catalytic layers were inspected by scanning electron microscopy (SEM) and characterised by energy-dispersive X-ray spectroscopy (EDX) and X-ray diffraction (XRD). XRD was carried out in an X'Pert Diffractometer (Phillips) using Cu-Kα radiation (energy line 0.15406 nm), tube power of 1.6 kW (40 kV at 40 mA), step size of 0.02° (300 s per step), and scan angle range of 5 to 90°. Nanostructured ZnO powder was used as a standard to perform Rietveld refinement and obtain the crystallite. XRD spectra peaks were identified using standard spectra from the Crystallography Opens Database (COD). SEM was carried out in a Quanta 650 FEG (Bruker) equipped with SE and BSE detectors. EDX analyses were made with a silicon drift detector (SDD) in a microanalysis system (Quantax, Bruker) coupled to the SEM system. All the analyses were carried out at the Laboratory for Technological Characterisation of the University of São Paulo (LCT/USP, Brazil).

Photocatalysis. Approximately 2 mL of the coated beads, ca. 3.7 g (SUS) or 1.5 g (glass), were carefully placed in the well inside the reactor with manual agitation to ensure a good distribution throughout the reactor volume in two layers. Glass wool was placed in the exit/entrance of the distribution channels to prevent channel blockage by the beads. The illumination window was installed afterwards. The assembled reactor was fed with an aqueous solution of acetaminophen (ACT) (99.9%, Sigma-Aldrich) at a concentration of 50-mg L^{-1} (3.3×10^{-4} mol L^{-1}), selected as a model pollutant, using a syringe pump (Elite 11, Harvard Apparatus) operating at three flow rates: 1.0, 0.8 and 0.2 mL min^{-1}, corresponding to space-times of 0.6, 0.7, and 2.9 min, respectively. The inlet solution has a natural pH of 6.8. The reactor was placed under monochromatic (365 ± 10 nm) UV-A radiation (100W LED array, Dongguan Hongke Lighting Co. Ltd.) with adjusted irradiance at 4.5 mW cm^{-2} at the reactor surface to simulate the UV component of sunlight at ground level, according to ASTM G173-3. The assembled reactors have an irradiation window of 15 cm^2, resulting thus in an irradiated power of 67.5 mW at the reactor surface. **Fig. 2** illustrates the experimental apparatus.

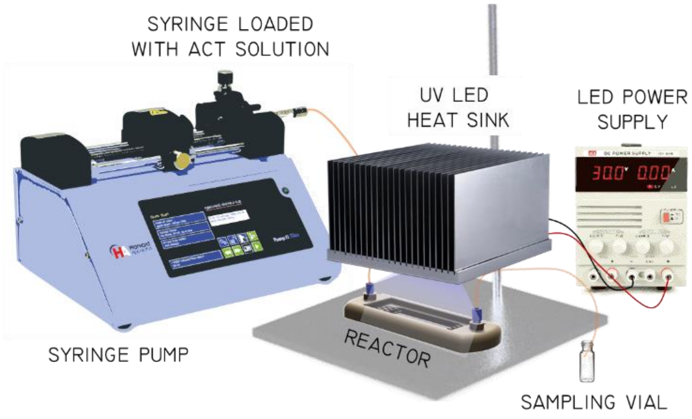

Fig. 2. Experimental setup for the photocatalysis experiments.

The model solution was pumped into the reactor at 1.0 mL min^{-1} for 60 min without illumination, and then for 60 min under illumination at each flow rate. 1.0-mL samples were collected every 30 min and analysed for their residual ACT content. The experiments were run three times for each packing spheres to analyse performance losses. Between each consecutive run, the reactor was disassembled; the beads were washed and dried in the laboratory oven before the next run. ACT was quantified by high-performance liquid chromatography (HPLC) with UV detection at 243 nm (LC20-A, Shimadzu Co.) after elution through a C18 column with a 0.8 mL min^{-1} 1:3 isocratic flow of methanol and deionised water.

4. RESULTS AND DISCUSSION

Reactor prototyping. The main results of the confocal microscopy are summarised in **Fig. 3**. Polished and unpolished (raw) sections of the bottom plates were analysed for their roughness profiles and the root mean square roughness, *Rq*. It was found that polishing (*Rq* = 916.4 nm ± 11.7%) promoted an average roughness reduction of about 20% compared with raw machined surfaces (*Rq* = 1127.1 nm ± 27.8%), resulting in a smoother profile with less extreme rugosity variation. This result showed that (i) ablation by CO_2 laser produces highly irregular surfaces and that (ii) sanding with rotating SiC wheels is an efficient technique for decreasing surface roughness. However, the final surface was not planar, with several instances of random waviness that made it difficult to ensure a regular distribution of the packing spheres.

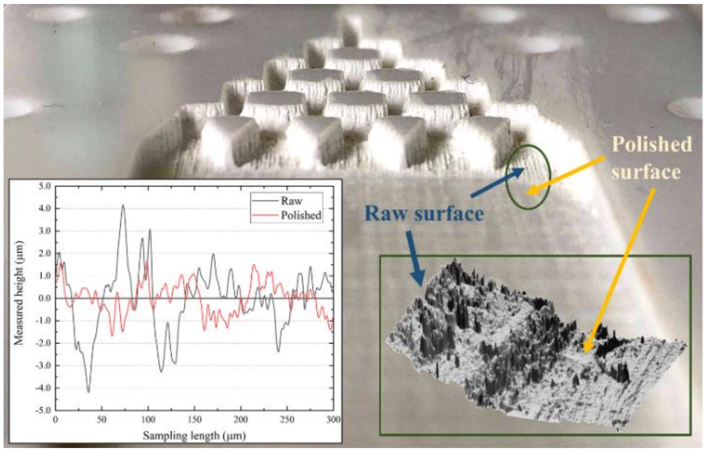

Fig. 3. Confocal microscopy analysis of finished surfaces machined by laser ablation after cleaning (*raw*) and post-processing by sanding (*polished*).

The lack of regularity of the ablated surfaces and the constant leakage problems found with these reactors led us to try a technique that provided more accurate dimensional control and eliminated the need of a complex sealing mechanism to make up the packed-bed reactors. **Table 2** shows a comparison between the dimensional accuracy and precision of the machining techniques adopted. It can be seen that FFF (i.e. 3D printing) resulted in facets with improved accuracy and precision compared with CO_2 laser ablation. One possible cause for the high deviations observed when using the latter technique is the skewness of the laser beam (McCreedy 2000; Lippert 2005). This leads to cone-shaped incisions which might cause excessive material accumulation near the walls, making engravings (e.g. channels) shorter and embossed structures (e.g. squares) larger than the target dimensions.

Table 2.
Comparison of dimensional precision and accuracy of prototypes obtained by CO_2 laser ablation (PMMA) and FFF (ABS), for selected facets of the design.

Target facet	Technique	Average* (mm)	STD*	Error (%)
3 × 3 mm square	Laser	3.102	± 5.6%	+3.4%
	FFF	3.002	± 3.5%	+0.1%
1.0 mm channel	Laser	0.894	± 16.3%	-10.6%
	FFF	1.209	± 6.8%	+2.9%

* Sampling size: 12 (square facets); 10 (channels).

The reactors prototyped by FFF have an average mass of 43 g, with a printing time of 4.8 h. Considering the materials spent and our location, the cost per reactor body was estimated at 4.80 BRL (ca. US$ 0.90).

Flow distributor design. The three proposed distributor geometries (**Fig. 1**) were studied using the laser-ablated prototypes.

Fig. 4 shows the exit-age distribution ($E(t)$) for the plate geometries and the observed wave-front patterns. The exit-age distribution is evaluated from the obtained concentration profile $C(t)$, according to Equation 1 (Fogler 2011):

$$E(t) = \frac{C(t)}{\int_0^\infty C(t)dt} \tag{1}$$

From this distribution, it is possible to calculate the *average residence time*, t_m, and the variance as follows:

$$t_m = \frac{\int_0^\infty t \times E(t)dt}{\int_0^\infty E(t)dt} = \int_0^\infty t \times E(t)dt \tag{2}$$

$$\sigma^2 = \int_0^\infty (t - t_m)^2 E(t)dt \tag{3}$$

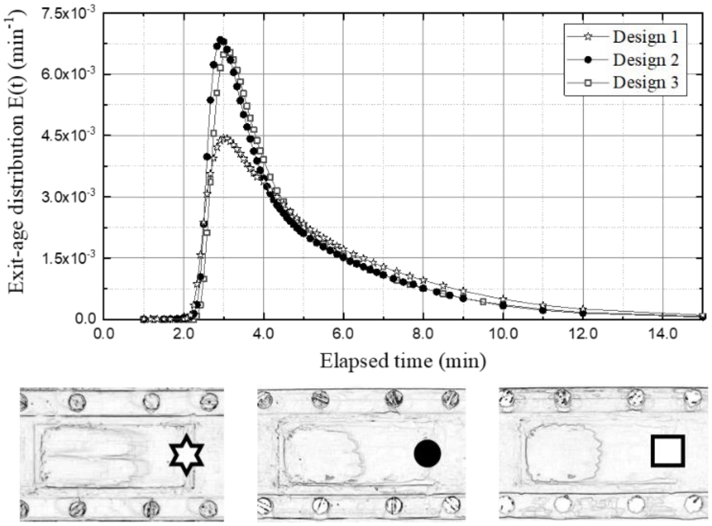

Fig. 4. Exit-age distributions and wave-front patterns observed in aqueous flow through the different prototyped designs (flow rate of 1 mL min^{-1}).

The wave-fronts shown in **Fig. 4** suggest that a simple flow distribution pattern (Design 1) is not sufficient to impart a plug-flow-like behaviour on the fluid in the middle section of the reactor, resulting in a broader $E(t)$ distribution (star-shaped marker curve), with a more pronounced CSTR behaviour. **Table 3** summarises the RTD results.

Table 3.
Summary of RTD results.

Design	t_m (min)	σ^2 (min^2)	τ (min)	t_m-τ
1	4.13	0.11	3.43	0.69

2	3.34	0.05	3.38	-0.04
3	3.47	0.05	3.36	0.10

These results show that Design 1 had a higher deviation from the expected residence time (the space-time, τ), another indication of a strong CSTR-like behaviour. Since this breaches guidelines D and E of our design rationale, designs 2 and 3 were considered for scaling out. Design 2 had a smaller deviation, and was chosen as basis for the reactors built in the next stages of the research.

Catalyst immobilisation. After the immobilisation procedure, the coated supports were analysed by XRD to confirm the nature of the deposited layer. **Fig. 5** shows the diffractograms for the ZnO samples coated onto SUS (A) and glass (B) substrates, compared with ZnO and other relevant standard spectra. The analysis proved challenging due to the geometry of the samples; nevertheless, it was possible to confirm the presence of ZnO, with a prevalence of the (1 0 0) orientation. The average crystallite size, calculated by Rietveld refinement, was estimated as 24.2 ± 1.8 nm in the SUS substrate, with a calculated density of 5.68 g cm^{-3}.

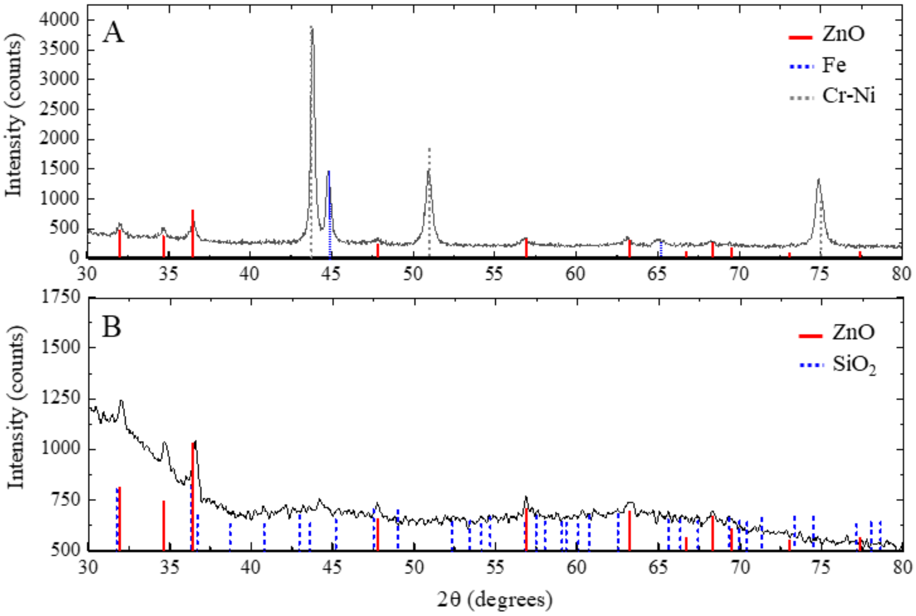

Fig. 5. X-ray diffractograms of the synthesised zinc oxide layers on (A) SUS and (B) glass substrates, with spectral lines of ZnO (solid vertical lines) and major substrate component standards (dashed vertical lines).

SEM-EDX analyses indicated average coverages of 57% (glass spheres) and 75% (SUS spheres). **Fig. 6 A** (glass) and **B** (SUS) show their surfaces, where it is possible to identify the contact points with neighbouring beads during synthesis. In these figures, the lighter patches indicate the presence of ZnO.

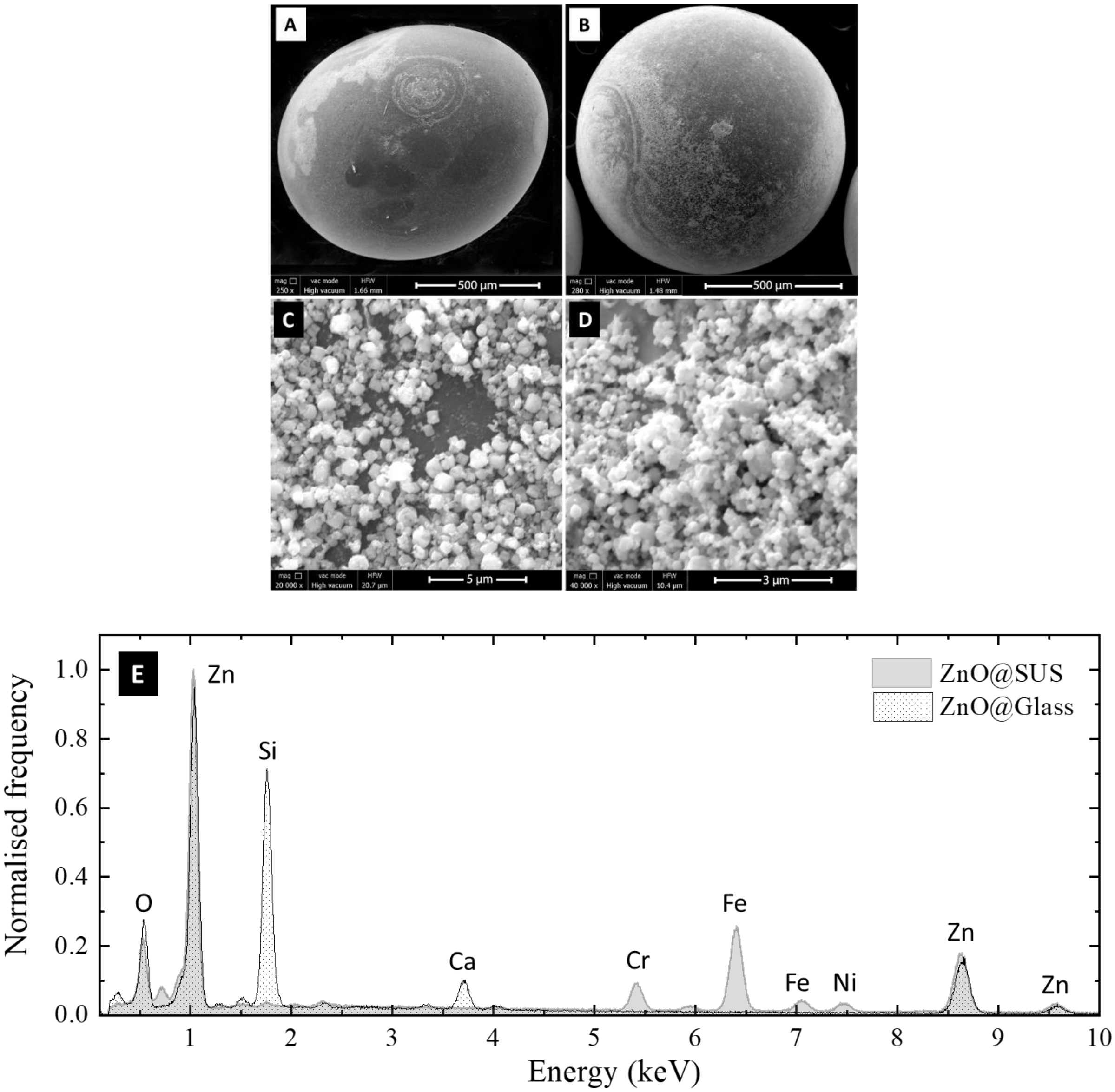

Fig. 6. SEM images of glass (A, C – with 250x and 20 000x magnification, respectively) and steel (B, D – with 280 and 40 000x magnification, respectively) spheres coated with ZnO. EDS spectra (20 keV) of coated portions of the beads are shown in E.

As shown in **Fig. 6 C**, the catalyst formed cylindrical structures (d_G = 630 ± 122 nm) on the surface of the glass beads, whereas on the SUS surface, the particles had less defined shapes and were substantially smaller (d_S = 337 ± 165 nm) (**Fig. 6 D**). The EDX spectra (**Fig. 6 E**) of coated sections of the beads confirmed the presence of ZnO in both supports.

The packed reactors had an internal volume of 1.8 ± 0.1 mL. Assuming a loose-packing configuration, the void fraction (ε) can be estimated as (Tidona et al. 2012):

$$\varepsilon = 0.37 + \frac{0.05 d_p}{D_h} + \frac{1.0867 d_p^2}{D_h^2} \tag{4}$$

where D_h is the equivalent hydraulic diameter of the flow cross-section, calculated from the cross-sectional area (A_{CS}) and perimeter (P_{CS}):

$$D_h = \frac{4A_{CS}}{P_{CS}} \tag{5}$$

The estimated void fraction – assumed same for all experiments – is of 46.6%, corresponding to a free interstitial volume of about 840 µL. The specific surface area of the bed (SSA_B) is calculated from the bed volume (S_V) by:

$$SSA_B = S_V(1-\varepsilon) \tag{6}$$

resulting in a SSA of ca. 3200 m^2 m^{-3}. The equivalent diameter of the insterstitial flow (D_{eq}) is ca. 580 µm, estimated using Eq. 7 (Rhodes 2008):

$$D_{eq} = \frac{4\varepsilon}{S_B} \tag{7}$$

Photocatalytic performance. The conversion profiles of the model pollutant (ACT) solution on the reactors are summarised in **Fig. 7**, for the reactor packed with stainless steel (SUS, square markers) and glass (G, triangle markers) beads. Each successive run (01, 02 and 03) is included in the figure.

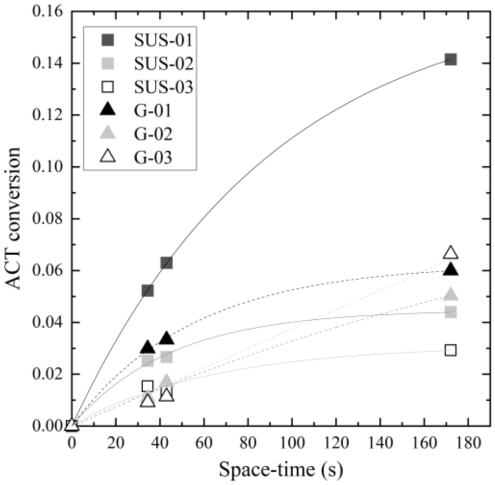

Fig. 7. Conversion of acetaminophen (ACT) achieved for each bed material and run, as a function of the space-time. $C_0 = 3.3 \times 10^{-4}$ M, pH = 6.9.

It can be seen from these results that stainless steel was more effective as catalyst support than glass in its first use. While some authors argue that this could be a result of Fe^{3+} ions segregation within the catalyst film (Yu et al. 2003), we could not confirm this ionic migration based on EDS and XRD analyses alone, although Fe, Cr and Mn peaks did appear in EDS analyses of ZnO-coated regions of the samples. Also, it is worth adding that the effect of the ionic segregation on the performance of the photocatalyst is still unclear, with other authors arguing that these ions actually hinder the photocatalytic activity by adding recombination centres (Fernández et al. 1995; Chen and Dionysiou 2006). From the perspective of our measurements, this improved performance is likely a result of the higher catalytic surface area available in the SUS bed, compared with the glass bed. Considering the void fraction and the initial coverage, the total covered area of the SUS beads was calculated at 4.81 m^2, whereas for the glass beads it was 24% smaller (3.65 m^2); this difference should be even larger in the actual catalytic surface area due to size of the coating structures. Nevertheless, it appears from our results that ZnO is more poorly fixed to steel than to glass, as can be inferred by the loss of activity after the first run. This is possibly a consequence of the synthesis methodology, which is more appropriate for glass and oxygen-rich substrates. The deposition in metals is more efficiently carried out by using seeding stages, as discussed elsewhere (Valde et al. 2012; Vu et al. 2013). A more quantitative discussion on the photocatalytic performance can be taken by evaluating the apparent rate constants, assuming a Langmuir-Hinshelwood mechanism (Fernández et al. 1995) can be used to describe the reaction kinetics as a function of the space-time, as described by Equation 8:

$$-\frac{dC}{d\tau} = \frac{k_r K_{ad} C}{1 + K_{ad} C} \tag{8}$$

where C is the concentration, τ is the space-time, k_r is the intrinsic reaction constant, and K_{ad} is the Langmuir adsorption constant. Considering the low concentration levels targeted in this work (order of magnitude of 10^{-4} mol L^{-1}) and typical adsorption values of aromatic organic species onto ZnO surfaces ($K_{ad} < 10$) (Xiong et al. 2016), it is safe to estimate that $K_{ad}C << 1$, hence Equation 8 can be simplified as:

$$-\frac{dC}{d\tau} = k_r K_{ad} C = k_{app} C \tag{9}$$

which can be integrated as:

$$\ln\left(\frac{C_0}{C}\right) = k_{app}\tau \tag{10}$$

where $k_{app} = k_r K_{ad}$ is the apparent first-order rate constant and C_0 is the concentration at the reactor inlet.

With this approximation, the values of k_{app} reported in **Table 4** were calculated. Three relevant observations can be derived from these data: (i) the uncertainty is higher for SUS packing, a reflection of the lower-quality of the data fitting (average R^2 = 0.88, compared with average R^2 = 0.995 for glass packing). This suggests that a different mechanism is taking place in the former case, in addition to Langmuir-Hinshelwood kinetics; (ii) it is also noticeable that the apparent rate constants lie within a comparable range after the first run, with a slightly better performance achieved using the glass beads; (iii) the efficiency loss of the SUS beads (ca. 70%) is clear from the values of k_{app}; and (iv) the apparent reaction rate constant seemed to increase with each reuse for the glass packing. To interpret this phenomenon, it is useful to compare these data with the curves in **Fig. 7**. At shorter space-times, the conversion is larger in the first runs ($\chi_1 > \chi_2 > \chi_3$); but the trend is reversed at longer space-times ($\chi_3 > \chi_2 > \chi_1$). This is could be due to the increased photon availability resulting from the loss of catalyst coverage. These additional photons can be used to activate catalytic sites previously largely inactive due to the scattering promoted by the ZnO coating in the upper layer of beads.

Table 4.

Apparent first-order rate constants evaluated for each packing condition.

Packing	k_{app} (× 10^{-4} s^{-1})	k/k_{max}	$t_{1/2}$ (min)
SUS-N1	9.47 ± 1.08 (11%)	1.00	12.2
SUS-N2	3.00 ± 0.70 (23%)	0.32	38.6
SUS-N3	1.91 ± 0.35 (18%)	0.20	60.6
Glass-N1	2.33 ± 0.06 (2%)	0.25	49.7
Glass-N2	3.06 ± 0.13 (4%)	0.32	37.8
Glass-N3	4.08 ± 0.13 (3%)	0.43	28.3

The apparent reaction rate constants experienced in reactors designed in this work are either comparable to or improved concerning reports from our peers for modified photocatalysts in a slurry configuration. For instance, Akkari et al. (2018) reported a k_{app} of 5.20 × 10^{-5} s^{-1} for ACT (C_0 = 50 mg L^{-1}) degradation under simulated solar irradiation using suspended ZnO (250 mg L^{-1}) in a batch reactor; while Miranda-García et al. (2011) reported a k_{app} between 9.0 and 15.8 × 10^{-4} s^{-1} for dilute ACT (C_0 = 0.1 mg L^{-1}) in a CPC packed-bed solar reactor, with TiO_2 immobilised onto 6.0-mm glass beads in recirculating batch operation. The improved reaction rates observed in our experiments can be attributed to the combination of the high SSA and narrow flow diameter of the beds – which reduce mass transport limitations and approximate the reaction rate to the intrinsic surface reaction, a feature commonly seen in microreactors (Ramos et al. 2015) – with improved illumination condition in comparison with slurry reactors. The mass transport quality in our reactors can be evaluated by the Sherwood number of the bed, given in Eq. 11 as a function of the Reynolds and Schmidt numbers, and the void fraction for packed-bed reactors (Gnielinksi 1980):

$$\mathrm{Sh} = \left(1 + 1.5(1-\varepsilon)\right)\left[2 + \sqrt{Sh_1^2 + Sh_2^2}\right]\text{, where} \tag{11-a}$$

$$Sh_1 = 0.664\,\mathrm{Re}^{\frac{1}{2}}\,\mathrm{Sc}^{\frac{1}{3}}$$

$$Sh_2 = \frac{0.037\,\mathrm{Re}^{0.8}\,\mathrm{Sc}}{1 + 2.443\,\mathrm{Re}^{-0.1}\,(\mathrm{Sc}^{2/3} - 1)} \tag{11-b}$$

$$\mathrm{Re} = \frac{\mathrm{Re_P}}{\varepsilon}$$

The Sherwood number represents the ratio of the total and the diffusive mass transfer rates and, as such, is an indicative of the effectiveness of mass transport in a given flow configuration (Levenspiel 2013). For the flow rates (0.1–1.0 mL min^{-1}) we investigated, the values of Sh were in the range of $7.7 < \mathrm{Sh} < 16.8$, comparable with the observed for highly efficient bed configurations (Kunii and Levenspiel 1991; Diniz et al. 2019).

Lastly, while he throughput we reported here were quite small, an interesting design feature of flat-plate reactors is that the processing rate can be scaled up by varying the dimensions of the irradiation window without appreciable loss in efficiency, provided the reactor depth (z_{bed}) and bed composition are not changed. The throughput (Q) can be evaluated as a function of the illuminated area (A_{illum}) as shown in Eq. 12:

$$Q = A_{illum}\, z_{bed}\, \frac{k_{app}}{\ln\left(\frac{C_0}{C}\right)} \tag{12}$$

We illustrate this scaling strategy in **Fig. 8**. This figure shows a design curve for a target ACT degradation of 80%, simulated using an average of the k_{app} reported in this work (2.4×10^{-4} s^{-1}) for a first-order conversion rate using Eq. 12. From this figure, we can estimate that for processing up to 200 L of effluent per day, a system with an equivalent irradiated area of 25 m^2 would be required. This could be provided by a piece of single equipment or by several smaller reactors connected in line.

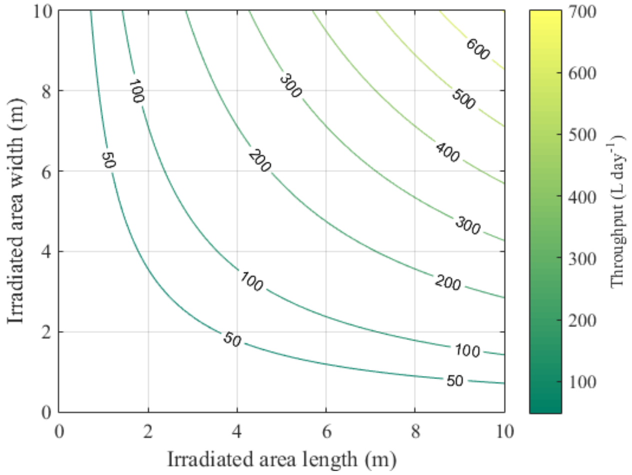

Fig. 8. Reactor design curve for a target conversion of 80%, considering the average k_{app} for reactors with ZnO-coated glass beads.

5. CONCLUSION

Reactor design is key for the efficient application of a complex multi-physical and heterogeneous system such as photocatalysis. It is a thriving field that can benefit from novel manufacture technologies, such as laser ablation and 3D-printing, as explored in this work. Using these technologies, we were able to manufacture reactors with dimensional accuracy between 90% (laser ablation) and 97% (FFF). Addressing the major limitations pointed out in the Design Rationale section, our reactors were packed with 1.0-mm beads, resulting in beds with an average SSA of 4300 m^2 m^{-3} and average equivalent flow diameter of 580 µm, leading to high apparent first-order reaction rate constants – in the order of 10^{-4} s^{-1} – about one order of magnitude higher than those found in conventional slurry batch reactors. Packed-beds made up from stainless steel performed better than glass (75% faster k_{app}) in the first use, as a consequence of the smaller particles in the catalytic layer ($d_S = 0.53\ d_G$) and higher coverage, which provided a covered area 24% larger; but they were strongly deactivated after the first use – whereas activity loss was not observed for the glass beads after three consecutive trials. We showed that this reactor configuration has efficient mass transport properties (Sh > 7.7) despite using fixed catalysts, and argued that this design can be easily scaled up by a simple scaling of the irradiated area.

DECLARATIONS

Ethics approval and consent to participate. Not applicable.

Consent for publication. Not applicable.

Availability of data and materials. The datasets used and/or analysed during the current study are available from the corresponding author on reasonable request.

Competing interests. The authors declare that they have no competing interests.

Funding. This work has received the support of the São Paulo Research Foundation (FAPESP grant 2018/21271-6) for equipment and material acquisition. The authors were supported by the São Paulo University Foundation (FUSP) and the National Council for Scientific and Technological Development (CNPq) with research fellowships. This study was financed in part by the Coordenação de Aperfeiçoamento de Pessoal de Nível Superior – Brasil (CAPES) – Finance Code 001 through provision of institutional infrastructure.

Authors' contributions. BR: Conceptualisation, methodology, data curation, formal analysis, writing – original draft; JGMC: Methodology, investigation; LIN: Methodology, investigation; ACSCT: Supervision, project administration, funding acquisition.

Acknowledgements. The authors would also like to acknowledge the support of the technicians G. Darin and Marco from the Laboratory of Technological Characterization of the University of Sao Paulo (LCT/USP).

References

Akkari M, Aranda P, Belver C, et al (2018) ZnO/sepiolite heterostructured materials for solar photocatalytic degradation of pharmaceuticals in wastewater. Appl Clay Sci 156:104–109. https://doi.org/10.1016/j.clay.2018.01.021

Aslan MH, Oral AY, Menşur E, et al (2004) Preparation of c-axis-oriented zinc-oxide thin films and the study of their microstructure and optical properties. Sol Energy Mater Sol Cells 82:543–552. https://doi.org/10.1016/j.solmat.2003.06.016

Au AK, Huynh W, Horowitz LF, Folch A (2016) 3D-Printed Microfluidics. Angew Chemie - Int Ed 55:3862–3881. https://doi.org/10.1002/anie.201504382

Beausoleil C, Yazdani Sarvestani H, Katz Z, et al (2020) Deep and high precision cutting of alumina ceramics by picosecond laser. Ceram Int 46:15285–15296. https://doi.org/10.1016/j.ceramint.2020.03.069

Braham RJ, Harris AT (2009) Review of major design and scale-up considerations for solar photocatalytic reactors. Ind Eng Chem Res 48:8890–8905. https://doi.org/10.1021/ie900859z

Chávez AM, Rey A, Beltrán FJ, Álvarez PM (2016) Solar photo-ozonation: A novel treatment method for the degradation of water pollutants. J Hazard Mater 317:36–43. https://doi.org/10.1016/j.jhazmat.2016.05.050

Chen PC, Zhang RH, Chen LT (2019) Using micromachined molds, partial-curing PDMS bonding technique, and multiple casting to create hybrid microfluidic chip for microlens array. Micromachines 10:. https://doi.org/10.3390/mi10090572

Chen Y, Dionysiou DD (2006) TiO2 photocatalytic films on stainless steel: The role of Degussa P-25 in modified sol-gel methods. Appl Catal B Environ 62:255–264. https://doi.org/10.1016/j.apcatb.2005.07.017

Diniz LA, Hewer TLR, Matsumoto D, Teixeira ACSC (2019) A comparison between the four Geldart groups on the performance of a gas-phase annular fluidized bed photoreactor for volatile organic compound oxidation. Environ Sci Pollut Res 26:4242–4252. https://doi.org/10.1007/s11356-018-2145-5

Ehrfeld W, Hessel V, Löwe H (2000) Microreactors. Wiley-VCH Verlag GmbH & Co. KGaA, Weinheim, Germany

Fernández A, Lassaletta G, Jiménez VM, et al (1995) Preparation and characterization of TiO2 photocatalysts supported on various rigid supports (glass, quartz and stainless steel). Comparative studies of photocatalytic activity in water purification. Appl Catal B, Environ 7:49–63. https://doi.org/10.1016/0926-3373(95)00026-7

Fogler (2011) Essentials of Chemical Reaction Engineering. Pearson Education Limited, New York

Gnielinksi V (1980) Waerme- und Stoff ubertragung in Festbetten. Heat Mass Transf 5:228–236

Khandarkhaeva M, Batoeva A, Sizykh M, et al (2019) Photo-Fenton-like degradation of bisphenol A by persulfate and solar irradiation. J Environ Manage 249:109348. https://doi.org/10.1016/j.jenvman.2019.109348

Kockmann N (2008) Transport Phenomena in Micro Process Engineering. Springer Berlin Heidelberg

Kumar SG, Rao KSRK (2017) Comparison of modification strategies towards enhanced charge carrier separation and photocatalytic degradation activity of metal oxide semiconductors (TiO 2 , WO 3 and ZnO). Appl Surf Sci 391:124–148. https://doi.org/10.1016/j.apsusc.2016.07.081

Kunii D, Levenspiel O (1991) Fluidization Engineering, 2nd edn. Butterworth-Heinemann, Stoneham

Levenspiel O (2013) The Chemical Reactor Omnibook. Lulu.com

Lippert T (2005) Interaction of photons with polymers: From surface modification to ablation. Plasma Process Polym 2:525–546. https://doi.org/10.1002/ppap.200500036

McCreedy T (2000) Fabrication techniques and materials commonly used for the production of microreactors and micro total analytical systems. TrAC - Trends Anal Chem 19:396–401. https://doi.org/10.1016/S0165-9936(99)00176-4

McCullagh C, Skillen N, Adams M, Robertson PKJ (2011) Photocatalytic reactors for environmental remediation: A review. J Chem Technol Biotechnol 86:1002–1017. https://doi.org/10.1002/jctb.2650

Miranda-García N, Suárez S, Sánchez B, et al (2011) Photocatalytic degradation of emerging contaminants in municipal wastewater treatment plant effluents using immobilized TiO2 in a solar pilot plant. Appl Catal B Environ 103:294–301. https://doi.org/10.1016/j.apcatb.2011.01.030

Nguyen VH, Wu JCS (2018) Recent developments in the design of photoreactors for solar energy conversion from water splitting and CO 2 reduction. Appl Catal A Gen 550:122–141. https://doi.org/10.1016/j.apcata.2017.11.002

Nogueira KRB, Nascimento CAO, Guardani R, Teixeira ACSC (2012) Feasibility Study of a Solar Reactor for Phenol Treatment by the Photo-Fenton process in Aqueous Solution. Chem Eng Technol 35:2125–2132. https://doi.org/10.1002/ceat.201200269

Ohtani B (2010) Photocatalysis A to Z-What we know and what we do not know in a scientific sense. J Photochem Photobiol C Photochem Rev 11:157–178. https://doi.org/10.1016/j.jphotochemrev.2011.02.001

Ramos B, Couri AP, Ookawara S, Teixeira ACSC (2018) Single-phase flow in a micro-structured packed bed photo-reactor : effect of packing size on flow regime and on the reactor performance for homogeneous photocatalysis. ChemRxiv Prepr 6726395:1–9. https://doi.org/10.26434/chemrxiv.6726395.v1

Ramos B, Ookawara S, Matsushita Y, Yoshikawa S (2015) Intensification of solar photocatalysis with immobilised TiO2 by using micro-structured reaction spaces. J Environ Chem Eng 3:681–688. https://doi.org/10.1016/j.jece.2015.03.016

Rhodes M (2008) Fluid flow through a packed bed of particles. In: Introduction to Particle Technology. John Wiley & Sons, Inc., p 450

Sculpteo (2019) The State of 3D Printing 2019 Edition. 26

Tidona B, Desportes S, Altheimer M, et al (2012) Liquid-to-particle mass transfer in a micro packed bed reactor. Int J Heat Mass Transf 55:522–530. https://doi.org/10.1016/j.ijheatmasstransfer.2011.11.012

Valde T, Marba G, Vu TT, Rı L (2012) Tailoring the synthesis of stainless steel wire mesh-supported ZnO. 47:1577–1586. https://doi.org/10.1016/j.materresbull.2012.02.017

Van Gerven T, Mul G, Moulijn J, Stankiewicz A (2007) A review of intensification of photocatalytic processes. Chem Eng Process Process Intensif 46:781–789. https://doi.org/10.1016/j.cep.2007.05.012

van Grieken R, Marugán J, Sordo C, Pablos C (2009) Comparison of the photocatalytic disinfection of E. coli suspensions in slurry, wall and fixed-bed reactors. Catal Today 144:48–54. https://doi.org/10.1016/j.cattod.2008.11.017

Vu TT, Río L, Valdés-solís T, Marbán G (2013) Stainless steel wire mesh-supported ZnO for the catalytic photodegradation of methylene blue under ultraviolet irradiation. J Hazard Mater 246–247:126–134. https://doi.org/10.1016/j.jhazmat.2012.12.009

Xiong S, Kong L, Zhong Z, Wang Y (2016) Dye adsorption on zinc oxide nanoparticulates atomic-layer-deposited on polytetrafluoroethylene membranes. AIChE J 62:3982–3991. https://doi.org/10.1002/aic.15293

Yu JC, Ho W, Lin J, et al (2003) Photocatalytic activity, antibacterial effect, and photoinduced hydrophilicity of TiO2 films coated on a stainless steel substrate. Environ Sci Technol 37:2296–2301. https://doi.org/10.1021/es0259483